Environmental Science
Water Research & Technology

ROYAL SOCIETY OF CHEMISTRY

PAPER

View Article Online
View Journal

Cite this: DOI: 10.1039/d2ew00209d

Treatment of emerging contaminants in simulated wastewater *via* tandem photo-Fenton-like reaction and nutrient recovery

Manoj Silva, [a] Mohamed Eisa, [a] Dovilė Ragauskaitė, [a] Madison H. McMinn, [b] Zhenyu Tian, [b] Clinton Williams,[c] Allan Knopf,[c] Lihua Zhang[d] and Jonas Baltrusaitis *[a]

Received 26th March 2022,
Accepted 30th November 2022

DOI: 10.1039/d2ew00209d

rsc.li/es-water

A tandem strategy that recovers NH_4^+ and PO_4^{3-} nutrients from simulated wastewater in a solid form after the Fenton oxidation of emerging organic contaminants was developed. Mesoporous Cu–MgO nanoparticles were used as a photo-Fenton-like catalyst to oxidize paraoxon and tetracycline present in nutrient-rich simulated wastewater to prevent their incorporation into the struvite product. Mesoporous MgO nanoparticles were subsequently used as the Mg-source for the struvite crystallization due to the fast intraparticle diffusion and adsorption kinetics facilitated by their porosity and the high surface area. Without Fenton oxidation, 13% of paraoxon and 37% of tetracycline were incorporated into the struvite, demonstrating the clear need for the removal of hazardous contaminants before struvite synthesis. Both organic contaminants were eliminated using the Fenton oxidation reaction, with some minor non-toxic intermediate products formed. The product formed after the tandem process was shown by XRD and Raman spectroscopy to be struvite free of the emerging organic contaminants.

Water impact

Emerging contaminants (ECs) pose a significant risk to the environment when they are incorporated into struvite recovered from nutrient-rich wastewater that contains such hazardous materials. By adding a heterogeneous Fenton oxidation pretreatment step, the ECs can be oxidized, and struvite recovery can be conducted without the risk of incorporating toxic contaminants.

1 Introduction

The use of modern mineral nitrogen and phosphorus fertilizers has led to an unprecedented productivity increase in the agriculture sector while also leading to significant perturbation of these nutrient cycles.[1–4] Nitrogen fixation *via* the Haber–Bosch process is used to produce ammonia, which subsequently is converted to urea, the most widely used nitrogen fertilizer in the world.[5] The inefficiency of urea use has been a topic of perennial importance as up to 90% of the applied nitrogen can be lost to leaching as runoff, or as greenhouse gas emissions.[6] The energy cost of nitrogen fixation is estimated to be 1–2% of the global energy consumption and 3–5% of the total natural gas output.[7] This energy loss caused by the inefficient utilization of fertilizer materials is an important sustainability concern.[8] In particular, the loss of nitrogen from urea as reactive nitrogen ($N_2O_{(g)}$, $NH_{3(g)}$, $NO_2^-{}_{(aq)}$, $NH_4^+{}_{(aq)}$) in the atmosphere and aquatic environment leads to adverse consequences such as climate change and algal blooms.[9] Similarly, phosphorous discharge in runoff has been identified as a significant driver of eutrophication resulting in aquatic life damage and significant methane emissions.[9,10] Provided that phosphorus is mined in a limited number of locations worldwide, the geopolitical implications of its future production are of concern.[11] Various wastewater streams of anthropogenic origin contain recoverable NH_4^+ and PO_4^{3-} with concentrations up to 1000 and 1500 mg L^{-1}, respectively.[12] Capturing these nutrients from wastewater in the form of struvite ($MgNH_4PO_4{\cdot}6H_2O$), a slow-release fertilizer, has been identified as a viable method toward a circular nutrient

[a] Department of Chemical and Biomolecular Engineering, Lehigh University, B336 Iacocca Hall, 111 Research Drive, Bethlehem, PA 18015, USA. E-mail: job314@lehigh.edu; Tel: +1 610 758 6836
[b] Department of Chemistry and Chemical Biology, Northeastern University, 02115, MA, USA
[c] USDA-ARS, US Arid Land Agricultural Research Center, 21881 N. Cardon Ln, Maricopa, AZ, 85138, USA
[d] Brookhaven National Laboratory, Center for Functional Nanomaterials, Upton, NY 11973, USA

economy that would alleviate negative environmental impacts of mineral fertilizers.[13–16] Struvite is synthesized by adding an Mg^{2+} source to NH_4^+ and PO_4^{3-} containing wastewater, with many studies focusing on the use of magnesium chloride. Recent studies showed that insoluble Mg-minerals such as MgO,[17–20] $MgCO_3$,[21] $CaMg(CO_3)_2$ (ref. 22–24) can also be used for struvite recovery as potentially more abundant and more sustainable sources, with PO_4^{3-} removal up to 94%.

The increasing presence of emerging contaminants (ECs) in wastewater poses a direct challenge for nutrient recovery due to the possible contamination of recovered solid fertilizer materials produced from wastewater-bearing pollutants such as pharmaceuticals, flame retardants, insecticides, herbicides and defoamers.[25] Such organic contaminants have been shown to affect the struvite crystallization process including crystal size and morphology.[26,27] An example has been reported where producing struvite from wastewater with the antibiotic tetracycline (TCL) present was shown to lead to its adsorption on the resulting struvite crystals.[28] Use of such contaminated struvite can lead to the alteration of the antibiotic resistome of soil and the rhizosphere.[29,30] Similarly, organophosphates are another increasingly common class of ECs that have detrimental effects on human health due to their environmental accumulation in soil, plants, and animal tissues.[31–34] Paraoxon-ethyl (*p*-OXN) has been reported to be a metabolite of parathion-ethyl, an organophosphate compound that is used as an insecticide.[35,36] Parathion is readily converted to paraoxon in the presence of sunlight.[37] The cholinesterase inhibition action of *p*-OXN renders it toxic to humans, while reports also show that exposure to even low doses of *p*-OXN can induce transgenerational effects.[36,38] Soil is a natural reservoir of both antibiotics and antibiotic-resistance genes, and as such, the addition of further antibiotic-containing compounds has severe consequences on the soil as well as crops grown in the contaminated soil.[39] The toxicity of ECs makes them recalcitrant toward traditional biological treatment and thus, they require harsher chemical oxidation treatments.[40] Advanced oxidation processes (AOPs) have emerged as a viable method of treating ECs, as the radicals produced during AOPs are powerful oxidizers capable of remediating toxic contaminants without hindrance.[41–43]

This study is focused on investigating a tandem process whereby the first stage utilizes the photo-Fenton-like reaction to degrade the ECs using Cu doped MgO nanoparticles (NPs) while in the second stage mesoporous MgO particles are used to synthesized struvite. First, equilibrium modeling was used to determine the Cu–MgO catalyst loading that would lead to high activity while avoiding struvite nucleation on the MgO support by using undersaturated conditions and to determine the optimal MgO loading used to recover struvite following the Fenton oxidation stages and catalyst removal. Next, EC incorporation in struvite was investigated without the Fenton oxidation step to confirm that TCL and *p*-OXN can contaminate the product struvite when nutrient recovery is conducted in the presence of ECs. Finally, the tandem process was tested with stage 1 as the Fenton oxidation stage, followed by catalyst separation and stage 2, where nutrient recovery with undoped MgO was conducted. The use of an AOP conducted at a neutral to alkaline pH environment ensured EC decomposition on the active copper metal center without leaching the metal into the aqueous phase. A semi-continuous injection of H_2O_2 was used to minimize the production of larger intermediate molecules as suggested in previous work.[44,45]

2 Materials and methods

2.1 Mesoporous Cu–MgO and undoped MgO nanoparticle synthesis

A facile thermal decomposition procedure was modified and used to synthesize undoped MgO NPs and 5% (by weight) Cu–MgO (ref. 22 and 30). Briefly, a solution of $Mg(NO_3)_2{\cdot}6H_2O$ (MilliporeSigma, 99%) and $Cu(NO_3)_2{\cdot}3H_2O$ (Sigma, 99+%) was prepared in methanol with the required mass ratios and a 0.59 M NaOH/methanol solution was added dropwise under reflux temperature. For the preparation of undoped MgO, $Cu(NO_3)_2{\cdot}2H_2O$ was omitted while keeping the same procedure. After 30 minutes of reaction at reflux temperature, the resulting precipitate was collected by centrifugation, washed three times using a 1:1 ratio of ethanol/water solution and dried at 80 °C overnight. The dry solid was calcined at 450 °C for 2 hours (2 °C min^{-1} ramp rate) in static air. Next, 0.5 g of the prepared material was added to 40 ml deionized water and stirred for 12 hours. After stirring, the gel was separated by centrifugation and dried at 80 °C. The sample was then calcined at 450 °C for 2 hours (2 °C min^{-1} ramp rate) in static air to obtain the final catalyst.

2.2 Photocatalytic degradation experiments

The *p*-OXN and TCL solutions were prepared by dissolving *p*-OXN (Acros Organics, 99+%) and TCL (Alfa Aesar, 91+%) in deionized water (Millipore). The concentrations for *p*-OXN and TCL were chosen to be 25 mg L^{-1}, consistent with previous literature reports discussing their presence in wastewater streams.[46,47] The catalyst concentration used was 250 mg L^{-1} (as discussed in section 3.1). A glass vessel containing 100 mL volume of EC solution was used in all experiments. In all experiments, an initial 20 mM dose of H_2O_2 was injected, followed by an additional 5 mM dose at 15 minute intervals. The vessel was irradiated by a 350 W xenon lamp (Newport), which provided an illumination intensity of approximately 100 mW cm^{-2}. 1 mL of solution was periodically filtered with a 0.22 μm membrane and measured HPLC to quantify EC concentration.

Ion chromatography (IC). The Metrohm Eco 925 IC system (Herisau, Switzerland) was used to measure the ion composition of the reacted solutions. Separation columns used were Metrosep A supp 4/5 Guard column (5 × 4 mm), Metrosep A supp 5 (4 × 150 mm) for anion analysis and Metrosep C 4 Guard column (5 × 4 mm), Metrosep C 4 (4 ×

150 mm) for cation analysis. The sample-loop volume was 10 μL in the cation system and 20 μL in the anion system, and eluted species were measured using a conductivity detector. Dipicolinic acid (1.75 nM HNO_3/0.7 mM) was used as an eluent for Metrosep C 4 while 3.2 mM Na_2CO_3/1.0 mM $NaHCO_3$ for Metrosep A supp 5. All samples were measured at room temperature. The system was controlled through MagIC Net 3.2 software.

High resolution mass spectrometry (HRMS). High resolution mass spectral analysis was performed on a Exploris 240 HESI-q-Orbitrap mass spectrometer (ThermoFisher Scientific). Samples were injected using a syringe pump at a rate of 5 μL min^{-1} to a T junction, where it met a solvent composition of 50% methanol with 0.1% formic acid/50% water with 0.1% formic acid (positive ion mode) or 50% methanol/50% 1 mM ammonium fluoride (negative ion mode) flowing at a rate of 0.1 mL min^{-1} from a Vanquish HPLC system (ThermoFisher Scientific) for tetracycline samples. For *p*-OXN, analysis was performed using the same conditions, but a mobile phase composition of 100% water with 0.1% formic acid (positive ion mode) or 100% 1 mM ammonium fluoride (negative ion mode).

Positive ion mode data was acquired using the following HESI source settings: spray voltage = 3500 V, sheath gas (Arb) = 50, aux gas (Arb) = 5, sweep gas (Arb) = 0, ion transfer tube temperature = 320 °C, and vaporizer temperature = 300 °C. For full scan MS^1, the following mass spectral settings were used: Orbitrap resolution (FWHM, at *m*/*z* 200) = 120 000, scan range = *m*/*z* 50–750, RF lens% = 60, AGC target = 100, source fragmentation = OFF. For fragmentation (MS^2) (tetracycline precursor ion = $[M + H]^+$ = *m*/*z* 445.1610; *p*-OXN precursor ion = $[M + H]^+$ = *m*/*z* 276.0632) the following mass spectral settings were used: isolation width = 0.4 *m*/*z*, HCD collision energy (absolute) = 17 V, all other settings were the same as full scan mode.

Negative ion mode data was acquired using the following HESI source settings: spray voltage = 3200 V, sheath gas (Arb) = 50, aux gas (Arb) = 5, sweep gas (Arb) = 0, ion transfer tube temperature = 320 °C, and vaporizer temperature = 300 °C. For full scan MS^1, the following mass spectral settings were used: Orbitrap resolution = 120 000, scan range = *m*/*z* 50–750, RF lens% = 120, AGC target = 100, source fragmentation = OFF. For fragmentation (MS^2) of (tetracycline precursor ion = $[M - H]^-$ = *m*/*z* 443.1461; *p*-OXN precursor ion = $[M - H]^-$ = *m*/*z* 274.0486) the following mass spectral settings were used: isolation width = 0.4 *m*/*z*, HCD collision energy (absolute) = 17 V, all other settings were the same as full scan mode.

Data was analyzed and figures were created in FreeStyle 1.8 SP2 (ThermoFisher Scientific). Mass spectral matching for tetracycline was done using m/zCloud (ThermoFisher Scientific).

2.3 Struvite synthesis

Simulated NH_4^+ and PO_4^{3-} containing wastewater samples were prepared by adding 1500 mg L^{-1} of monoammonium phosphate (MAP), $NH_4H_2PO_4$ (99.9%+, Fisher Scientific) in 18.2 MΩ cm^{-1} deionized water (Millipore, USA). A 1500 mg L^{-1} MAP solution represents PO_4^{3-} and NH_4^+ values found in municipal, animal and industrial wastewater[12] while maintaining above the molar 1 : 1 ratio needed for struvite formation. MgO NPs were added to 500 mL of the simulated wastewater and stirred for up to 120 minutes. Aliquots of 0.5 mL were sampled periodically, filtered through a 0.22 μm polyethersulfone filter, and analyzed using ion chromatography. The MgO concentration used for struvite synthesis was 750 mg L^{-1}, which corresponds to molar $[Mg^{2+}]:[NH_4^+]:[PO_4^{3-}]$ ratio of 1.44 : 1 : 1. $[Mg^{2+}]:[NH_4^+]:[PO_4^{3-}]$ ratios of 0.5–1.5 : 1 : 1 have previously been tested and was concluded that lower ratios lead to a lesser N and P adsorption/reaction.[18,48,49] Therefore, a slight excess of Mg^{2+} was preferred in the previous works to circumvent this issue and ensure efficient removal of N and P from the solution.[50,51] The kinetics of adsorption were analyzed using the pseudo-second order equation (eqn (1)).[52]

$$t/q_t = 1/k_2 q_e^{\ 2} + t/q_e \quad (1)$$

The pseudo-second order rate constant is denoted by k_2 (g_{MgO} $mg_{PO_4}^{-1}$ min^{-1}), the adsorbed PO_4 concentration at time *t* (min) is denoted by q_t (mg_{PO_4} g_{MgO}^{-1}), and the adsorbed PO_4 concentration at equilibrium is denoted by q_e (mg_{PO_4} g_{MgO}^{-1}).

For struvite synthesized in the presence of ECs, a solution containing 25 mg L^{-1} of the EC (either TCL or *p*-OXN) and 1500 mg L^{-1} MAP was prepared. To this solution, 750 mg L^{-1} of MgO NPs were added to produce struvite. For the tandem process (shown in Fig. 1), the Cu–MgO catalyst used in the oxidation step was first removed *via* filtration, and following catalyst removal, 750 mg L^{-1} of MgO NPs were added to the solution to initiate struvite formation.

Saturation index (SI) calculations. Visual Minteq 3.1 software was used to calculate SI values of the potential solid products at equilibrium.[53] The pH in each case was varied over the range measured during each experiment. The ionic strength was not fixed but rather calculated from the ion balance. Concentrations of 250 mg L^{-1} of NH_4^+ and 1250 mg L^{-1} PO_4^{3-} were held constant in all calculations while the Mg^{2+} ion concentration was set to that of the Mg from the initial MgO and the Mg^{2+} measured from the aqueous phase to study phosphate adsorption and homogeneous nucleation. A temperature of 25 °C was used to mimic experimental conditions.

2.4 Struvite physicochemical characterization

Powder X-ray diffraction. The crystal structure of all catalysts was confirmed using powder X-ray diffraction (Empyrean, PANalytical B.V.). The applied current was 40 mA and the applied voltage was 45 kV. The X-ray mirror that was used was a graded, flat Bragg–Brentano HD mirror, with the step size set to 0.0131 degrees.

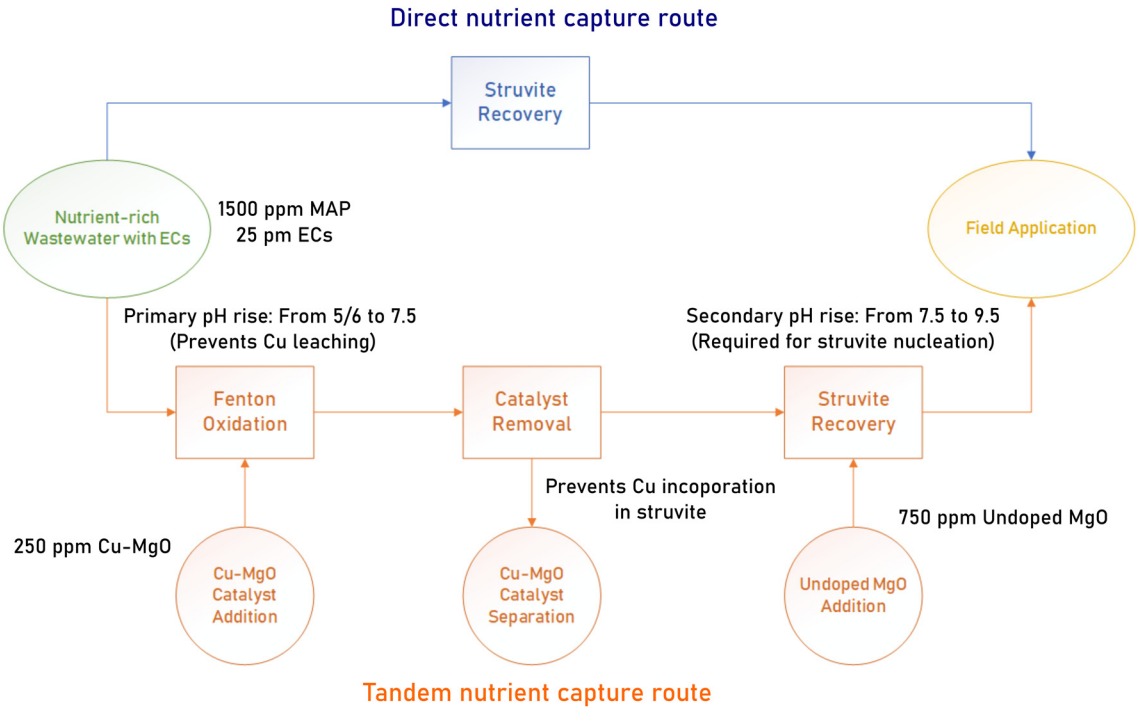

Fig. 1 Graphical representation of the tandem photo-Fenton-like oxidation and subsequent nutrient recovery process studied in this work.

Raman spectroscopy. Horiba-Jobin Yvon LabRam HR (high-resolution) spectrometer equipped with a 442 nm laser. The laser was focused through a confocal microscope with a 50× objective (Olympus BX-30-LWD). Before spectra were collected, the Raman spectrometer was calibrated with a silicon standard possessing a reference band at 520.7 cm^{-1}. The spectral resolution of the spectrometer is ~1 cm^{-1}, and the spectra were collected with 600 grating, 5 scans (30 s per scan) and a 100 μm pinhole.

Scanning electron microscopy. All SEM images were obtained using a Hitachi 4300 SE FE-SEM. A 5.0 kV voltage setting was used with an aperture setting of 3 and a gun brightness of 1.

3 Results and discussion

3.1 Physicochemical characterization of Cu–MgO NPs

The photo-Fenton-like oxidation of the selected ECs using mesoporous Cu–MgO NPs was proposed recently.[45] The use of such basic solid catalysts that operate in neutral to alkaline environments has been demonstrated to lead to catalyst operation free of metal leaching in the aqueous phase.[45,54,55] Fig. 2 shows a summary of the physicochemical characterization of as-synthesized Cu–MgO with emphasis on the crystal structure and pore textural properties. As shown in Fig. 2(a), the XRD pattern for the 5% Cu–MgO contains all the major peaks corresponding to MgO, while several minor peaks are present matching those of CuO. Specifically, the region between 2θ angles 30–40° displayed peaks corresponding to (0 0 2), (−1 1 1), (2 0 0), and (1 1 1) of CuO in addition to MgO peaks.[56–58] Cu and Mg have similar ionic radii (73 and 72 Å, respectively) and this causes both the solid solution of MgO and CuO as well as a separate CuO nanoparticle phase to form in this catalyst.[56,57] The mesoporous structure of the catalyst material is evident from the type IV isotherm observed by nitrogen physisorption

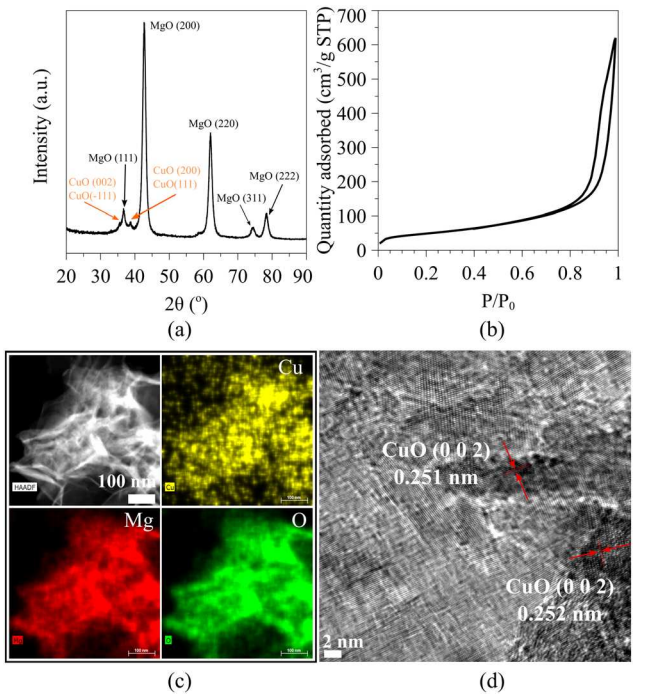

Fig. 2 Cu–MgO characterization (a) XRD pattern (b) nitrogen physisorption isotherm (c) STEM-EDS maps (d) HR-TEM image for 5% Cu–MgO.

shown in Fig. 2(b). The surface area for the Cu–MgO NPs was measured to be 170 $m^2\ g^{-1}$ with 0.974 $cm^3\ g^{-1}$ pore volume. The high surface area and porosity facilitate faster intraparticle diffusion, leading to faster reaction kinetics.[54] Fig. 2(c) and (d) show HAADF STEM-EDS and HR-TEM images for the Cu–MgO nanoparticles. Cu dispersion over the MgO is evident in HAADF-STEM-EDS, while the HR-TEM allowed for *d*-spacing to be measured, confirming the presence of CuO nanoparticles dispersed over the MgO support. The CuO (0 0 2) *d*-spacing was measured to be between 0.251–0.252 nm.[59] Previous work on Cu–MgO NPs utilized XANES to confirm that CuO was present in the as-synthesized catalysts and that CuO was the sole phase of Cu in the as-synthesized catalysts.[20]

3.2 Equilibrium-based modeling of precipitate phase speciation

The precipitation of struvite and other magnesium phosphate phases is determined by a combination of the pH of the solution, as well as the activity of the ion species that comprise the various possible precipitates. While struvite is the desired product of the nutrient recovery process, various magnesium phosphate phases such as $MgHPO_4{\cdot}3H_2O$ and $Mg_3(PO_4)_2{\cdot}22H_2O$ and the hydroxide phase brucite ($Mg(OH)_2$) can also precipitate depending on the thermodynamic favorability of formation.[18] The most useful thermodynamic parameter that can model the equilibrium distribution of precipitates as a function of pH and ion activity is the SI.[60,61] Visual Minteq was used to model the SI as a function of pH and Mg^{2+} ion concentration in the solution to guide the experimental design. In equilibrium simulations of struvite recovery, it was assumed that nearly all of the Mg^{2+} is available due to enhanced transport rates facilitated by the higher surface area and more efficient intraparticle diffusion in mesoporous MgO.

Fig. 3 shows the saturation indices as a function of pH and Mg^{2+} concentration for struvite, $Mg(OH)_2$, $Mg_3PO_4{\cdot}22H_2O$, and $MgHPO_4{\cdot}3H_2O$. Indeed, the solution pH remains under 7.5 when the Cu–MgO concentration is <300 mg L^{-1},

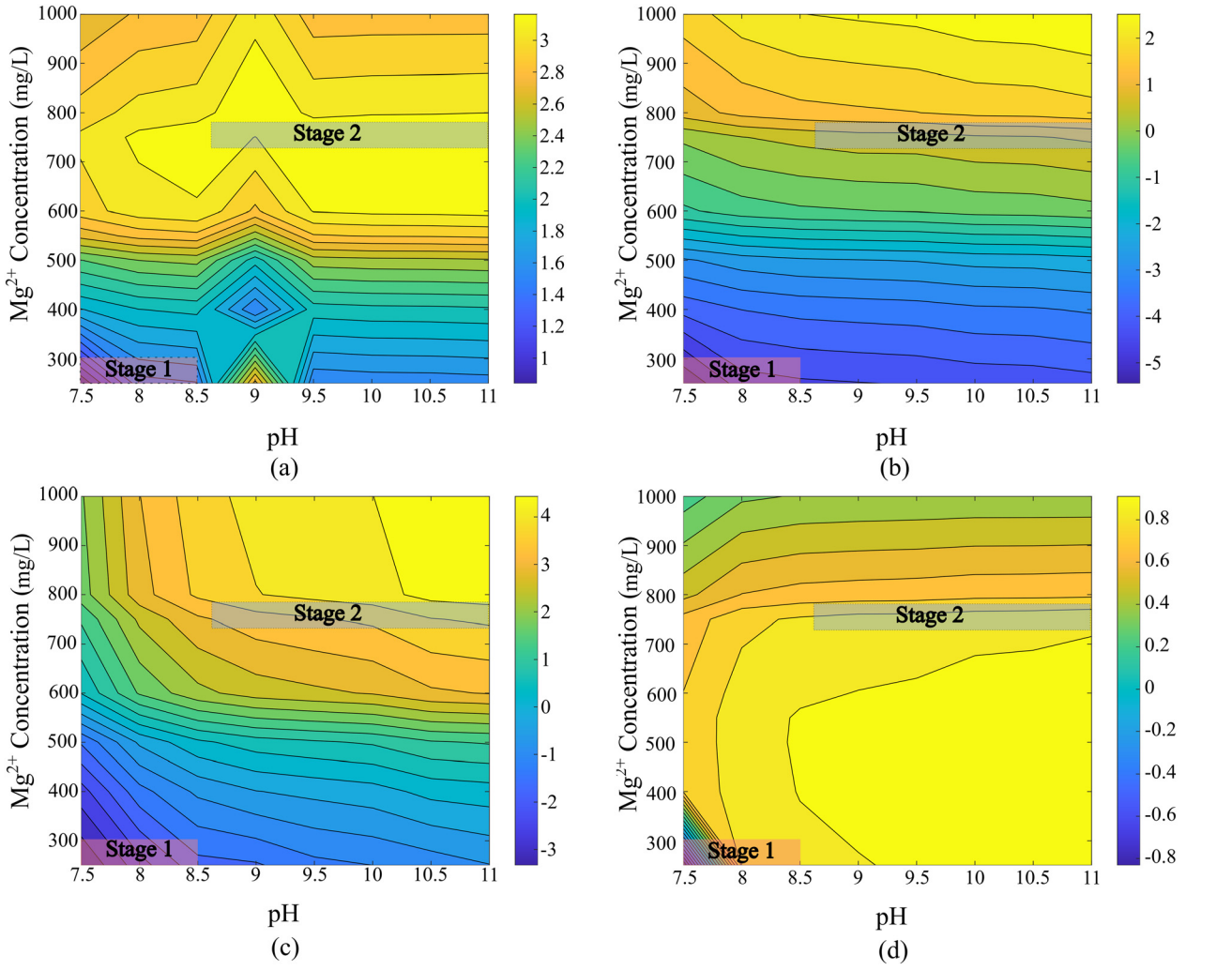

Fig. 3 SI for (a) struvite (b) brucite (c) $Mg_3PO_4{\cdot}22H_2O$ (d) $MgHPO_4{\cdot}3H_2O$ as a function of pH and Mg^{2+} concentration in the aqueous phase (SI shown by the color bar).

which results in saturation indices being near zero or negative (highlighted area for stage 1 in Fig. 3). This agrees with previous work where the 0.44 : 1 : 1 ratio of Mg^{2+} : NH_4^+ : PO_4^{3-} not producing struvite (or other precipitates).[18] This undersaturated condition is desired since the NH_4^+ and PO_4^{3-} are not expected to adsorb on the catalyst, which allows the Fenton oxidation to proceed without perturbing the nutrients in the solution.

A Mg^{2+} : NH_4^+ : PO_4^{3-} the ratio of 1.44 : 1 : 1 is the optimal ratio for struvite synthesis from MgO with no detectable magnesium phosphate by-product formation with no external pH control as reported previously on both microcrystalline and nanostructure MgO.[18,20] Higher ratios (such as 4.8 : 1 : 1) were shown to produce magnesium phosphate phases that did not contain NH_4^+.[18,20] This behavior has been reported for other insoluble Mg-sources such as dolomite ($CaMg(CO_3)_2$)[22] and magnesite ($MgCO_3$).[21] The pH value is desired to be in the 7.5–10 range for struvite crystallization. Following catalyst separation, undoped MgO is added as the Mg-source for struvite recovery. This addition of MgO leads to the rapid rise of pH above 9, which causes the SI for struvite and $Mg_3PO_4{\cdot}22H_2O$ become higher than 1, indicating supersaturation. For the MgO concentration of ~750 mg L^{-1}, the saturation indices for $Mg(OH)_2$ and $MgHPO_4{\cdot}3H_2O$ show that these phases are not thermodynamically favored to be major products, as their saturation indices are significantly lower than struvite or $Mg_3PO_4{\cdot}22H_2O$. Between struvite and $Mg_3PO_4{\cdot}22H_2O$, it can be seen that the saturation indices vary between 2.8 and 3.3 and that the struvite SI is slightly higher in the 7.5–9.5 pH range at 750 mg L^{-1} of MgO loading. As the pH increases beyond 10 and higher MgO loadings (up to 1000 mg L^{-1}) are present, the $Mg_3PO_4{\cdot}22H_2O$ SI value increases beyond that of struvite, indicating that the dominant phase at higher pH values and higher MgO loadings would be $Mg_3PO_4{\cdot}22H_2O$. This is consistent with previous studies reporting PO_4^{3-} adsorption kinetics over a larger range of MgO loadings and pH values.[18,20,21] Therefore, pH control and MgO loading selection become important considerations in the process design of struvite recovery, as these two parameters can determine the product speciation. While the struvite SI is only slightly higher than the SI for $Mg_3PO_4{\cdot}22H_2O$ during this stage, it is important to consider that Visual Minteq models the thermodynamic products, without considering kinetic products. Therefore, in the critical region of struvite growth (the initial 10 minutes where the rapid pH rises from 7.5 to 9.5 occurs), struvite is most likely to be kinetically favored to precipitate, even though $Mg_3PO_4{\cdot}22H_2O$ is also thermodynamically favored to precipitate, but is not found to be a major product kinetically.[18]

3.3 Effects of ECs on struvite production during direct nutrient capture route

Before studying the tandem process of Fenton oxidation and struvite recovery, the effect of ECs on struvite crystallization was studied separately to understand how EC incorporation occurs in the absence of Fenton oxidation before struvite crystallization (the direct nutrient capture route presented in Fig. 1). In this study, simulated wastewater consisting of 1500 mg L^{-1} MAP and 25 mg L^{-1} of ECs was used to produce struvite using undoped MgO as the Mg-source. Struvite crystallization was initiated by adding 750 mg L^{-1} of MgO NPs to a 1500 mg L^{-1} MAP solution in the dark. The experiment was conducted in the dark to avoid light-induced reactions involving the ECs.[54] The 750 mg L^{-1} MgO loading was used as this was expected to reach the desired SI value consistent with the highlighted stage 2 region in Fig. 3(a). Fig. 4(a) shows the relative concentrations of the ECs during struvite synthesis with simultaneously measured total-*P* concentration for three experiments: no ECs present, TCL, and *p*-OXN. The *p*-OXN and TCL show 13% and 37% relative concentration reduction over a 2 hour reaction time, demonstrating that both contaminants can be incorporated into the product struvite. Therefore, the need for a pretreatment step of oxidizing the ECs before struvite formation becomes critical, as struvite contaminated with ECs leads to significant environmental hazards.[28,29] In all three cases (no ECs, *p*-OXN, and TCL), the PO_4^{3-} removal remains high, with 99%, 97%, and 95%, respectively. Fig. 4(b) shows the pseudo-second order kinetic analysis results for the three cases of forming struvite: namely without ECs and the two scenarios with TCL and *p*-OXN. The adsorbed phosphate concentrations from the initial 30 minutes of the reaction were fitted to the pseudo-second order equation as the reaction approaches equilibrium within the first 30 minutes. The pseudo-second order equation was used since previous work on MgO has shown that the data with a higher quality of fit compared to the pseudo-first order, and since the pseudo-first order equation is more applicable to systems where the bulk adsorbate concentration does not vary significantly.[10,18,62] The phosphate concentrations during the first 30 minutes of reaction were fitted to the pseudo-second order equation to calculate the rate constant and phosphate adsorbed at equilibrium. Since phosphate adsorption on mesoporous MgO rapidly approaches equilibrium, with the majority of the phosphate adsorbed within the first 10 minutes, fitting to the first 30 minutes becomes sufficient.[20] The k_2 values for the no ECs present, TCL, and *p*-OXN experiments were calculated to be 0.01 g mg^{-1} min^{-1}, 0.0015 g mg^{-1} min^{-1}, 0.0022 g mg^{-1} min^{-1}, respectively. The concentration of phosphate adsorbed at equilibrium or q_e values were calculated to be 1640 mg g^{-1}, 1597 mg g^{-1}, and 1611 mg g^{-1}, respectively. The first 30 minutes of phosphate adsorption show a kinetic hindrance when ECs are present, but the equilibrium phosphate removal achieved after 2 hours of reaction does not show a large variation. However, the EC incorporation when struvite is formed in the presence of TCL and *p*-OXN shows the need for the photo-Fenton-like oxidation stage.

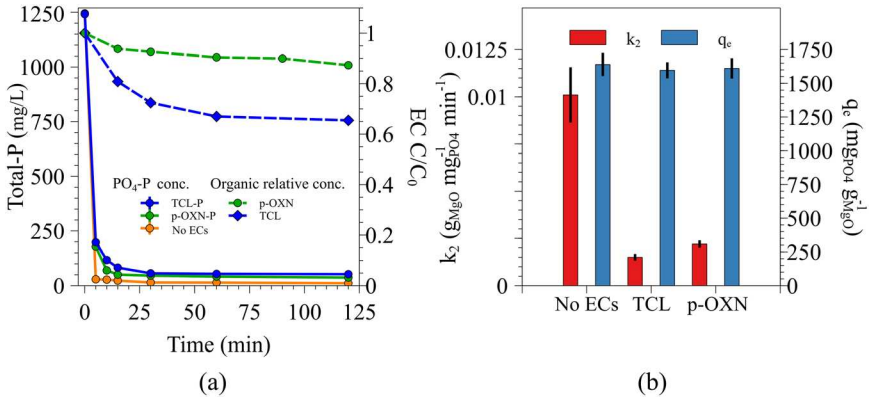

Fig. 4 (a) EC relative concentrations (dashed lines) and total-*P* concentration (solid lines) over time during struvite synthesis in the presence of ECs (b) pseudo-second order rate constant and equilibrium adsorbed PO_4^{3-} concentration for control and in the presence of ECs.

3.4 Photo-Fenton-like catalysis of ECs using Cu–MgO NPs

The propensity of Cu–MgO particles to oxidize the two ECs of interest was first established. The Cu–MgO catalyst concentration was chosen to be 250 mg L^{-1} for the photo-Fenton-like oxidation reaction of ECs based on the SI calculations, as 250 mg L^{-1} Cu–MgO does not lead to any precipitation of struvite due to the undersaturated conditions as discussed in section 3.2. The photo-Fenton-like oxidation was first studied in the absence of MAP in the solution. Fig. 5(a) and (b) show the relative concentrations of *p*-OXN and TCL, respectively (C/C_0 where C denotes the concentration at time t, and C_0 denotes the initial concentration of 25 mg L^{-1}). The parent structures of the ECs are broken down completely within the first 5 minutes of reaction, as both species show a rapid decrease by the 5 minute time point. The overall reaction time for both ECs was 2 hours due to prior literature on TCL, and in the case of *p*-OXN, the MS spectra showed no change past 2 hours of reaction (further discussed in section 3.5). The measured *p*-OXN and TCL concentrations after 120 minutes of reactions were 0.00 mg L^{-1} and 0.02 mg L^{-1}, respectively, which corresponds to over 99% conversion in both cases.

Further, to understand the fate of the heteroatoms N and P in TCL and *p*-OXN, experiments were conducted where 25 mg L^{-1} of TCL and *p*-OXN were reacted with 250 mg L^{-1} Cu–MgO and IC were used to measure the concentration of NH_4^+ and PO_4^{3-} over the reaction time. Fig. 5(c) shows the inorganic ion concentrations for these two experiments. Importantly, within the first 5 minutes of reaction, the NH_4^+ and PO_4^{3-} resulting from heteroatoms in each respective EC reached the stoichiometric value expected if all of the N and P were converted to NH_4^+ and PO_4^{3-}, respectively. These ions can also be recovered with the nutrients already present in their ionic form in wastewater.

3.5 Semi-continuous H_2O_2 delivery for photo-Fenton-like oxidation

As discussed in the section above, the Cu–MgO catalyst led to the complete oxidation of the parent structures of TCL and *p*-OXN, and the liberation of the heteroatoms as NH_4^+ and PO_4^{3-} for TCL and *p*-OXN, respectively. While the parent structures were eliminated, various smaller intermediate species can be present in the solution. Previous work on using the heterogeneous Fenton reaction to remediate ECs has shown that to minimize the amount of intermediate a semi-continuous H_2O_2 delivery should be used instead of a single dose, as this ensures a constant presence of H_2O_2 in the solution that can be activated to produce radicals.[44,45] As

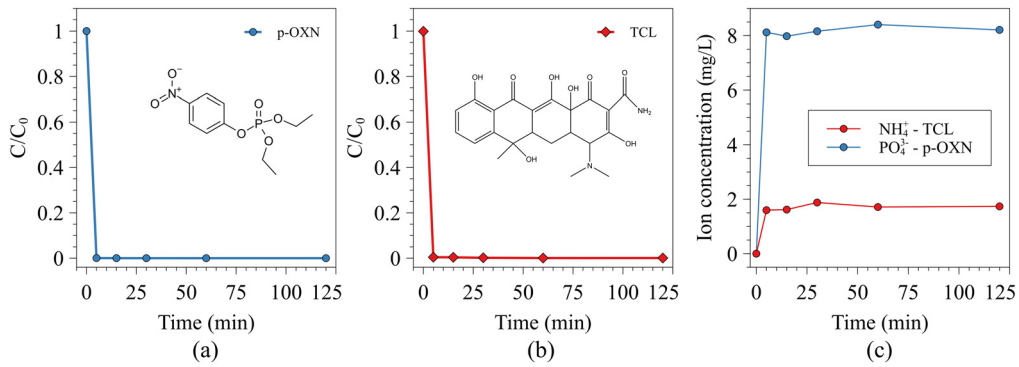

Fig. 5 The relative concentration of ECs as a function of the reaction time under the photo-Fenton-like reaction phase for (a) *p*-OXN (b) TCL. (c) Inorganic ions (the N and P in TCL and *p*-OXN, respectively), are liberated during the reaction and measured as NH_4^+ and PO_4^{3-} using IC.

the number of intermediates are reduced to smaller molecules, the toxicity of the solution compared to the parent molecules has been shown to dramatically decrease, and achieve non-toxicity.[46,63] A previous study using the Cu–MgO and a single dose of H_2O_2 at the beginning of the reaction revealed that a larger distribution of products would be present after the reaction due to inefficient utilization of H_2O_2.[45] Therefore, the Fenton reaction in this study utilizes this semi-continuous H_2O_2 delivery, and time-resolved mass spectrometry was used to monitor the intermediates in the solution.

As shown in Fig. 6, high-resolution mass spectrometry (HRMS) was used to investigate the degradation of TCL and *p*-OXN in MAP at different timepoints of the Fenton oxidation (0, 15, 60 and 120 minutes). *p*-OXN and TCL were detected in the 0 min solution in both positive and negative ion mode, however detection of *p*-OXN and TCL in addition to any resulting degradation products was limited in negative ion mode and will not be discussed in detail. TCL in both positive and negative ion mode was shown to be fully degraded within 15 minutes (Fig. 6a). With the degradation of TCL, there is an emergence of low *m*/*z* species in the 15,

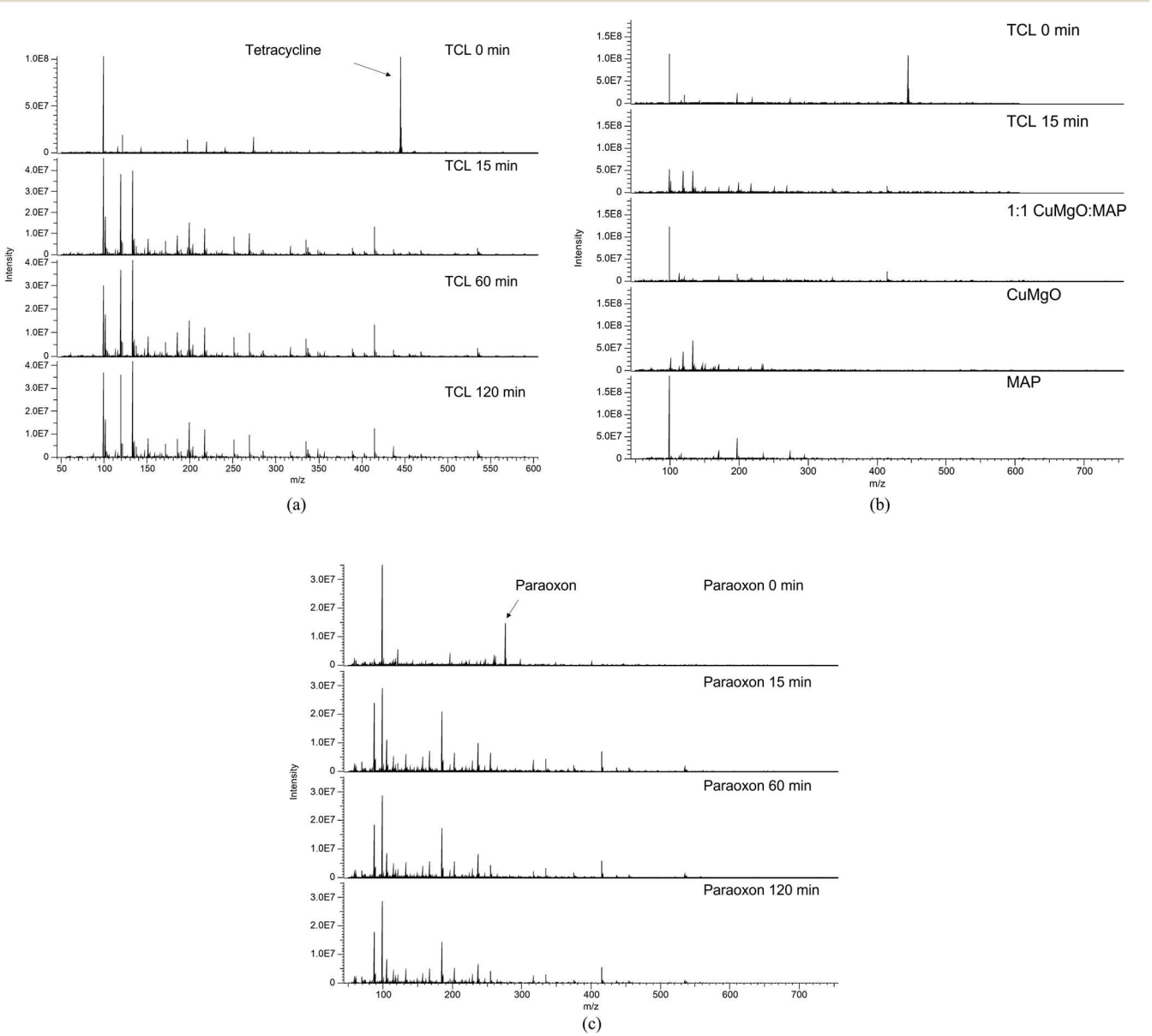

Fig. 6 Time-resolved MS spectra for (a) TCL during the photo-Fenton-like oxidation (250 mg L^{-1} Cu–MgO catalyst + 25 mg L^{-1} TCL + 20 mM initial H_2O_2 dose followed by 5 mM doses at 15 minute intervals). (b) High resolution mass spectra comparison of TCL (untreated 0 min, treated 15 min), and blank controls (1 : 1 CuMgO: MAP, CuMgO, and MAP). (c) *p*-OXN during the photo-Fenton-like oxidation (250 mg L^{-1} Cu–MgO catalyst + 25 mg L^{-1} *p*-OXN+ 20 mM initial H_2O_2 dose followed by 5 mM doses at 15 minute intervals).

60, and 120 minute samples. However, upon further investigation the majority of these ions can be traced back to MAP and the MgO catalyst (Fig. 6b). Identification of degradation products was challenging by HRMS due to the presence of ammonium and phosphate ions from the MAP, which may be contributing to ion suppression and masking the presence of any TCL degradation products. Analysis was further complicated by the presence of with Mg^{2+} ions from the MgO catalyst, resulting in the formation of $[M + Mg]^+$ adducts in the resulting mass spectra. The presence of Mg adducts was determined based on isotope fine structure, due to the natural abundance of Mg isotopes resulting in a unique M + 1 and M + 2 pattern. Another reason as to why degradation products are not readily observed is that by the 15 minute mark TCL had undergone complete mineralization into products not detectable by HRMS. Two potential degradation products of TCL were identified in positive ion mode (m/z 185.0057 = $C_4H_{10}O_3P + Mg_2$ and m/z 184.9695 = $CH_6O_7P + Mg$). Similar observations were made for analysis of *p*-OXN. *p*-OXN was found to be fully degraded after 15 minutes (Fig. 6c). Detection of *p*-OXN in negative ion mode was limited at all timepoints, and there were no notable degradation products observed. In positive ion mode, while upon initial evaluation there appears to be numerous degradation products, once subjected to MS^2 it becomes clear that the major peaks are Mg clusters of several very small molecules, suggesting that *p*-OXN also underwent mineralization.

Alternatively, previous work has shown that TCL breaks down into linear acids such as oxalic (m/z = 90), acetic (m/z = 60), and malonic (m/z = 103) acids using heterogeneous Fenton like reactions.[64] These linear acids do not pose the toxicity risks that are presented by the parent molecules, or some of the larger intermediates reported to be found in other reports.[46,63] Unambiguous detection of these linear acid products, however, is not possible due to the overlapping peaks due to the catalyst matrix shown in Fig. 6b.

The oxidation of ECs using oxygen radicals is a multi-step process due to the cleavage of the various C–H, C–C, C–O, C–N bonds, which leads to ECs being broken down into smaller intermediate molecules, before being mineralized to CO_2 and H_2O, along with other inorganic ions that are produced due to the presence of heteroatoms such as N and P. Previous work using Cu–MgO has demonstrated that both $^{\bullet}OH$ radicals and $HO_2^{\bullet}/^{\bullet}O_2^-$ radicals are involved in the degradation of ECs.[45] TCL has been studied in multiple previous reports, and several of the intermediate molecules have been identified.[46,63–65] The ROS generated by the catalytic activation of H_2O_2 causes the scission of C–C and C=C bonds, which cause the aromatic rings of TCL and *p*-OXN to be broken to produce both smaller aromatic products and linear products.[66] For TCL, previous studies have proposed degradation pathways where the initial 4 benzene rings are cleaved step-wise to produce intermediates containing 1–3 rings, while also removing all N atoms from the TCL parent structure.[66]

3.6 Tandem photo-Fenton-like oxidation of ECs and subsequent nutrient recovery

As previous sections have established that 1) ECs can incorporate into struvite during direct nutrient capture with no EC oxidation (shown in Fig. 4) 2) the Cu–MgO catalyst can potentially oxidize the ECs to linear acids with no toxicity risks (section 3.5), a tandem process of oxidizing the ECs first and then recovering nutrients *via* struvite crystallization is proposed. For stage 1 where the Fenton oxidation occurs, a 250 mg L^{-1} loading of Cu–MgO is used, as SI calculations show this would not lead to struvite crystallization as the solution remains undersaturated, but the catalyst provides sufficient activity to oxidize ECs. Following catalyst separation, stage 2 utilizes 750 mg L^{-1} undoped MgO to initiate struvite recovery, as the pH increase from MgO dissolution and the increased concentration of MgO provides the correct SI for struvite formation (highlighted stage 2 area in Fig. 3(a)). The cation and anion concentration, as well as the solution pH, are shown in Fig. 7 for the tandem process where the first 120 minutes show the ion concentrations and pH overtime for the Fenton oxidation step (plot area highlighted in blue), and the subsequent 120 minutes are for struvite recovery which occurs after the catalyst is removed and undoped MgO is added to the solution. As shown in Fig. 7, the PO_4^{3-} and NH_4^+ concentrations remain constant over the photo-Fenton-like oxidation stage. In both cases of *p*-OXN and TCL, the pH increases rapidly in the first 15 minutes following the addition of the Cu–MgO catalyst due to the surface hydration of the MgO support.[48,67] Previous work on MgO has shown that water diffuses into the pores and hydrates the surface to produce $Mg(OH)^+_{(surface)}$ and $OH^-_{(aq)}$, which causes the pH to rise.[48,68] The $Mg(OH)^+_{(surface)}$ and Mg^{2+} ions close to the surface, recombine with OH^- to produce an overlayer of $Mg(OH)_2$, which terminates further dissolution of the surface and stabilizes the pH in the range of 7.2–7.5 in this study.[48,68,69] Overtime slight depression of the pH is observed due to dissolution of CO_2 from the atmosphere, but this effect is not significant over short periods.[48] The second pH rise occurs due to the addition of undoped MgO, which acts as the Mg-source for struvite precipitation. Since the second phase uses a slight excess of MgO, an immediate decrease in PO_4^{3-} and NH_4^+ concentrations due to struvite formation. The pH in the second phase rises to the range from the range of 7.2–7.5 to the range of 9.3–9.8 in the first 15 minutes following MgO addition and attains a final pH of 9.9–10.

The pH control provided by the MgO support dissolution during the photo-Fenton-like oxidation stage provides the important advantage of preventing Cu from leaching into the aqueous phase.[45] During the second phase which is nutrient recovery, the increased pH is necessary to induce struvite precipitation, as the typical pH range of 7–9.5 is required.[18,51,70] Fig. 7(a) and (b) depict the cation concentrations and the pH over the reaction time. At the end of the 2 hour nutrient recovery phase, 87% NH_4^+ removal was

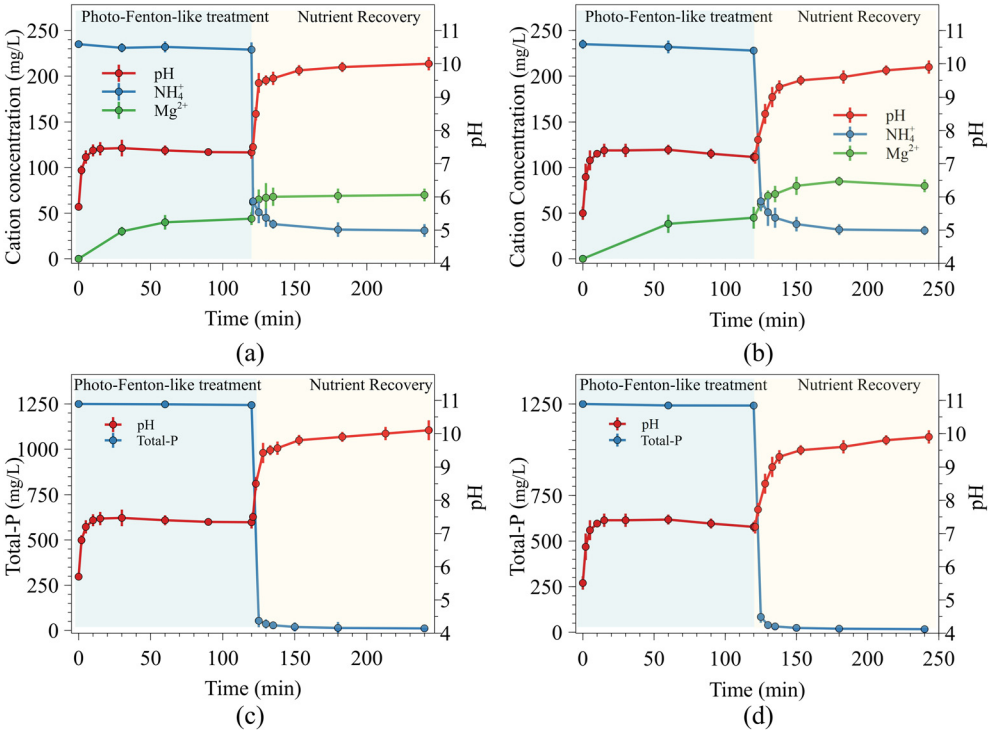

Fig. 7 Cation (NH_4^+ and Mg^{2+}) concentrations (mg L^{-1}) and pH of the solution as a function of time during the tandem AOP and nutrient recovery process with (a) *p*-OXN (b) TCL. Total-*P* concentration (mg L^{-1}) and pH of the solution as a function of time during tandem AOP and nutrient recovery process with (c) *p*-OXN (d) TCL.

observed in both cases where *p*-OXN and TCL were pretreated with the photo-Fenton-like reaction. The residual Mg^{2+} concentration after the 2 hour struvite recovery phase in the *p*-OXN case was 70 mg L^{-1}, while the TCL case showed 80 mg L^{-1}. Fig. 7(c) and (d) show the total-*P* concentration and the pH of the solution over the reaction time. After the 2 hour reaction time, both the *p*-OXN and TCL pretreated experiments yielded 99% total-*P* removal. This total-*P* removal is consistent with previous work on mesoporous MgO.[20] Compared to microcrystalline MgO, the rate of adsorption is highly enhanced in mesoporous MgO due to the faster intraparticle diffusion facilitated by the mesopore structure.[18,20] Previous work on MgO supported on porous supports such as diatomite has also demonstrated similar enhanced kinetics, but with the disadvantage of incorporating the support in the struvite product.[70,71]

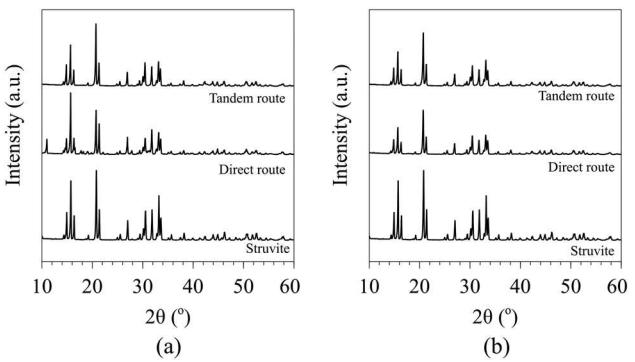

Fig. 8 XRD patterns for struvite formed using the (a) direct route in the presence of *p*-OXN and the tandem route (b) direct route in the presence of TCL and the tandem route.

3.7 Struvite product physicochemical characterization

The crystal structure of the produced struvite samples was studied using powder XRD. Fig. 8 shows the XRD patterns for struvite formed without any ECs, struvite recovered in the presence of ECs (direct nutrient capture route), and struvite recovered using the tandem route. In all cases the dominant XRD pattern was the struvite pattern, indicating that the major crystalline product is struvite (PDF #15-0762).[72] This has been demonstrated to be the case in previous work using both mesoporous MgO NPs and microcrystalline MgO.[18,20] As shown in Fig. 8(a), the XRD patterns for struvite formed in the presence of *p*-OXN, and the struvite formed following the photo-Fenton-like catalytic oxidation contain a minor peak at 11°. This peak is attributed to a small quantity of $Mg_3(PO_4)_2{\cdot}22H_2O$ present (PDF #35-0186) in struvite. At high pH and high concentrations of PO_4^{3-} the formation of $Mg_3(PO_4)_2{\cdot}22H_2O$ becomes thermodynamically stable as shown by SI calculations, which leads to the crystalline product being a mixture of struvite and $Mg_3(PO_4)_2{\cdot}22H_2O$, with $Mg_3(PO_4)_2{\cdot}22H_2O$ being the minor product.

Fig. 9 shows select SEM images and size distributions for the struvite crystals formed in the presence of the ECs using

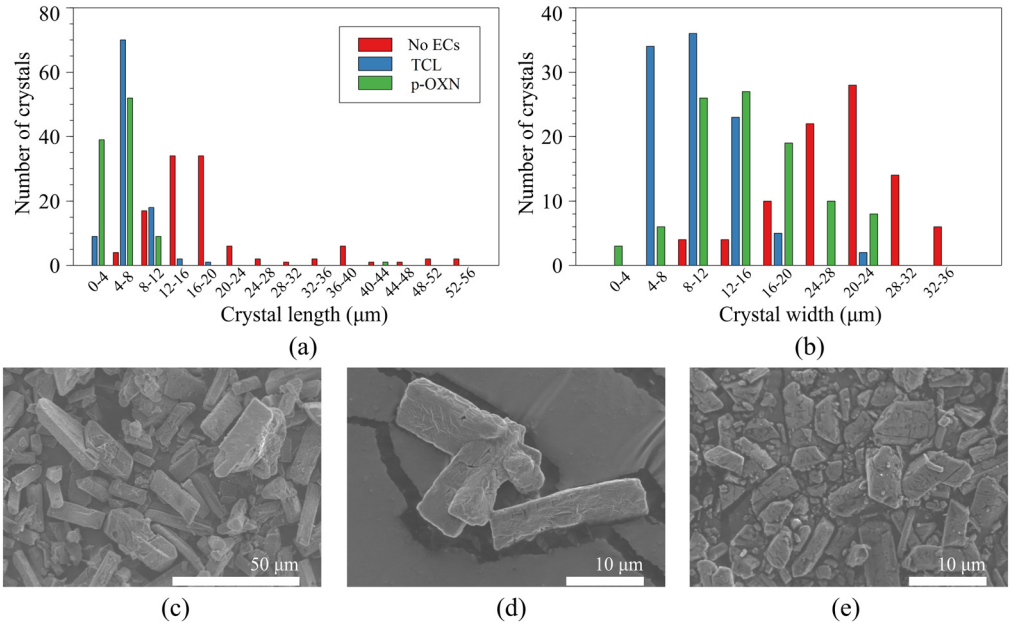

Fig. 9 Size histograms for struvite crystals in the presence of organic contaminants (a) crystal length (b) crystal width. Select SEM images for (c) struvite formed with no ECs present (d) struvite formed using the direct route in the presence of *p*-OXN (e) struvite formed using the direct route in the presence of TCL (histogram generated using measurements from 100 individual crystals).

the direct nutrient capture route. The purpose of the size distribution analysis of struvite crystals formed in the presence of ECs was to identify whether the distribution crystal lengths and widths would be altered due to the presence of ECs. As shown in Fig. 9(a) and (b), the average crystal length and width are reduced in the presence of ECs. The production of smaller crystals in the presence of dissolved organic matter has been reported in previous literature.[51] The N release rate from struvite is dependent on crystal size in the initial 6 weeks after application, with smaller crystals releasing more N due to higher exposed surface area.[73,74] Therefore, controlling struvite crystal size has important implications on its application, and thus, producing struvite in a solution with less organic matter would be beneficial. The characteristic rod-shaped struvite crystals are present in the SEM images shown in Fig. 9(c)–(e).

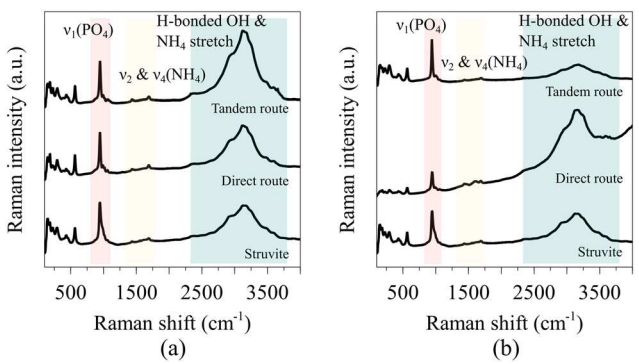

Fig. 10 Raman spectra for struvite (a) with *p*-OXN and post-Fenton oxidation (b) with TCL and post-Fenton oxidation.

Raman spectra for the produced struvite crystals are shown in Fig. 10. In all three cases, the major struvite peaks were evident, confirming the XRD finding that struvite is the major crystalline product for each scenario. Fig. 10(a) shows the Raman spectra for the control struvite sample, struvite formed in the presence of *p*-OXN, and the struvite formed following the Fenton oxidation of the solution containing *p*-OXN. All three spectra show the same major peak positions. Fig. 10(b) shows the Raman spectra for the control struvite sample, struvite formed in the presence of TCL, and the struvite formed following the Fenton oxidation of the solution containing TCL. In all cases the $\nu_1(PO_4)$ stretch for struvite is located at 946 cm^{-1}, while the ν_4 mode corresponds to 560 cm^{-1}.[75,76] The hydrogen-bonded hydroxyl/water and ammonium species lead to the rise of a prominent region, with broadband centered around 3124 cm^{-1} and a shoulder around 2950 cm^{-1}.[77,78] Struvite contains tetrahedral NH_4^+ groups, as evidenced by the 1435 cm^{-1} and 1690 cm^{-1} peaks.[77,78] The struvite sample formed in the presence of TCL showed laser-induced fluorescent behavior during analysis, resulting in a sloping baseline. Such fluorescence can be observed due to chromophores in the sample that are excited to a higher electronic state such as the conjugated rings of TCL adsorbed on the struvite crystals, which results in radiation emitted that is larger than that of the Raman signal of interest.[79] Previous literature on struvite synthesis in the presence of ECs such as TCL has shown that the contaminant can incorporate into or adsorb onto the struvite crystal to varying degrees depending on the exact chemical identity of the ECs.[28,80] The struvite samples formed in the presence of *p*-OXN remained the white color observed in the control sample as the *p*-OXN solution was colorless, while the

struvite synthesized in the presence of TCL obtained the orange color present in the TCL solution. While the Raman spectrum for the struvite containing TCL contained largely the same major peaks present in the pure struvite, one additional minor peak was evident at 1603 cm^{-1} was observed. This peak has been assigned in literature to C–C stretches as well as C–O bends and is the major TCL peak in the 1700–600 cm^{-1} region.[81–83] Other TCL peaks in this region have very low intensities, and as such, were not detected in this analysis.[81,83] Therefore, the 1603 cm^{-1} peak is not definitively assigned to TCL in this work. The low concentration of adsorbed ECs provides low-intensity signals which are easily overcome by the higher intensity of Raman signal coming from the crystalline struvite, and thus, detecting adsorbed ECs using Raman spectroscopy becomes challenging.

3.8 Ca^{2+} concentration effects on NH_4^+ adsorption and the resulting solid product formation

Finally, we investigated the Ca^{2+} ion, commonly found in wastewater, effects on NH_4^+ ion removal during the nutrient recovery phase in a 2-step process using TCL and *p*-OXN post-Fenton oxidation solution. In Fig. 11a and b, it can be seen that for both TCL and *p*-OXN NH_4^+ ion removal directly correlates with Ca^{2+} concentration in an aqueous solution. In particular, increasing Ca^{2+} concentration decreases NH_4^+ ion removal. The apparent reason for this phenomenon can be inferred from Fig. 11c where a complex mixture of the solid product was obtained using XRD, differently from Fig. 8 where only struvite was observed. Two additional observations can be made from Fig. 11c. A non-struvite peak at ~2θ = 11° transitioned to 12° with the increasing Ca^{2+}

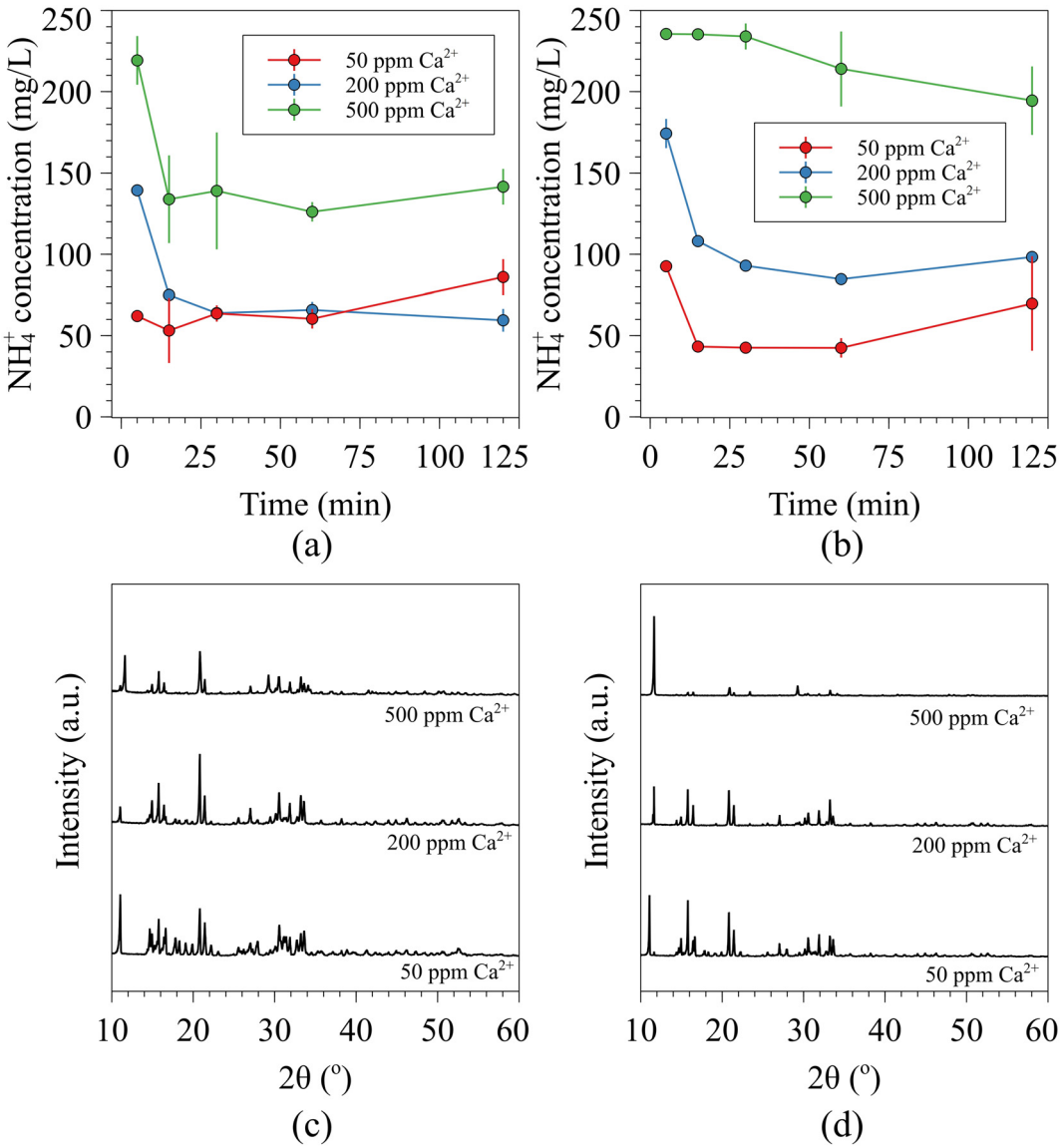

Fig. 11 Aqueous NH_4^+ ion composition profile for (a) TCL and (b) *p*-OXN post-Fenton oxidation during the nutrient recovery phase in the 2-step process shown in Fig. 1 with 750 mg L^{-1} of MgO NPs added to the solution to initiate struvite formation. In (c) XRD patterns are shown for the solid products as a function of Ca^{2+} concentration resulting from (a) while in (d) – from (b). $CaCl_2$ was added as calcium source at 50, 200 and 500 ppm Ca^{2+}.

content. Additionally and somewhat unexpectedly, the complex mixture of the solid products changed with the increasing Ca^{2+} content to that of pure struvite shown in Fig. 8 and a strong peak due to the hydrated magnesium phosphate at $\sim 2\theta = 12°$. This improvement in the observed struvite crystallinity is also observed in Fig. 11d where a strong $2\theta = 12°$ peak is complemented by a minor struvite amount since the adsorption of NH_4^+, as shown in Fig. 11b, decreases at 500 ppm Ca^{2+}. Fig. 11 suggests that Ca^{2+} has a significant effect on NH_4^+ adsorption from post-Fenton oxidation solutions using 750 mg L^{-1} of MgO NPs with the major product shifting to magnesium phosphate. Notably, the peak at $2\theta = 12°$ could not be associated with any major calcium solids, such as $CaCO_3$ or $Ca(OH)_2$.

4 Conclusions

Struvite recovery provides a unique opportunity to remove nutrients from wastewater that would cause eutrophication and produce a value-added chemical that can be used as a green fertilizer. However, the presence of ECs in water has introduced an additional challenge to struvite recovery, given that these contaminants can adsorb on the struvite crystals and cause various environmental issues during field application. Both *p*-OXN and TCL were shown to adsorb on struvite crystals up to 13% and 37% when struvite was produced directly from wastewater containing these two ECs, illustrating the importance of eliminating ECs from wastewater before nutrient recovery. This study shows a tandem process in treating the ECs in nutrient-laden wastewater with a photo-Fenton-like reaction step as a pretreatment before nutrient recovery *via* struvite crystallization, to extract nutrients in the form of a green fertilizer without the risk of EC incorporation. The photo-Fenton-like reaction using a Cu–MgO catalyst was shown to be effective in eliminating the parent structures of *p*-OXN and TCL, reducing the risk of toxicity. Using equilibrium modeling, the Cu–MgO catalyst loading was chosen to achieve sufficient activity, while ensuring the solution remains undersaturated, preventing struvite precipitation. Following the Fenton oxidation stage and catalyst separation, the nutrient recovery was conducted by adding undoped MgO, the loading of which was guided by the SI calculations to selectively produce struvite as the major crystalline product. Product characterization using XRD and Raman revealed that struvite is produced as the major product and that while struvite and $Mg_3PO_4{\cdot}22H_2O$ were both predicted to precipitate by equilibrium modeling, struvite forms as a kinetically favored product. SEM analysis showed that the particle size distribution of struvite is altered by ECs, as struvite formed in the presence of ECs yielded finer crystals.

Conflicts of interest

The authors declare no conflicts of interest.

Acknowledgements

This material is based upon work supported by the National Science Foundation under Grant No. CHE 1710120. The authors acknowledge Dr. Bar Mosevitzky Lis for assistance in obtaining Raman data.

References

1 J. A. Foley, R. Defries, G. P. Asner, C. Barford, G. Bonan, S. R. Carpenter, F. S. Chapin, M. T. Coe, G. C. Daily, H. K. Gibbs, J. H. Helkowski, T. Holloway, E. A. Howard, C. J. Kucharik, C. Monfreda, J. A. Patz, I. C. Prentice, N. Ramankutty and P. K. Snyder, *Science*, 2005, **8**, 570–574.
2 J. A. Foley, N. Ramankutty, K. A. Brauman, E. S. Cassidy, J. S. Gerber, M. Johnston, N. D. Mueller, C. O'Connell, D. K. Ray, P. C. West, C. Balzer, E. M. Bennett, S. R. Carpenter, J. Hill, C. Monfreda, S. Polasky, J. Rockström, J. Sheehan, S. Siebert, D. Tilman and D. P. M. Zaks, *Nature*, 2011, **478**, 337.
3 J. N. Galloway, A. R. Townsend, J. W. Erisman, M. Bekunda, Z. Cai, J. R. Freney, L. A. Martinelli, S. P. Seitzinger and M. A. Sutton, *Science*, 2008, **320**, 889–892.
4 B. E. Rittmann, B. Mayer, P. Westerhoff and M. Edwards, *Chemosphere*, 2011, **84**, 846–853.
5 J. N. Galloway and E. B. Cowling, *Ambio*, 2002, **31**, 64–71.
6 J. N. Galloway, J. D. Aber, J. W. Erisman, S. P. Seitzinger, R. W. Howarth, E. B. Cowling and B. J. Cosby, *Bioscience*, 2003, **53**, 341–356.
7 J. Baltrusaitis, *ACS Sustainable Chem. Eng.*, 2017, **5**, 9527.
8 D. E. Canfield, A. N. Glazer and P. G. Falkowski, *Science*, 2010, **330**, 192–196.
9 J. J. Beaulieu, T. DelSontro and J. A. Downing, *Nat. Commun.*, 2019, **10**, 1375.
10 M. Silva and J. Baltrusaitis, *Environ. Sci.: Water Res. Technol.*, 2020, **6**, 3178–3194.
11 B. K. Mayer, L. A. Baker, T. H. Boyer, P. Drechsel, M. Gifford, M. A. Hanjra, P. Parameswaran, J. Stoltzfus, P. Westerhoff and B. E. Rittmann, *Environ. Sci. Technol.*, 2016, **50**, 6606–6620.
12 T. Cai, S. Y. Park and Y. Li, *Renewable Sustainable Energy Rev.*, 2013, **19**, 360–369.
13 M. Smol, *J. Mater. Cycles Waste Manage.*, 2019, **21**, 227–238.
14 H. P. Jing, Y. Li, X. Wang, J. Zhao and S. Xia, *Environ. Sci.: Water Res. Technol.*, 2019, **5**, 931–943.
15 P. Kehrein, M. van Loosdrecht, P. Osseweijer, M. Garfí, J. Dewulf and J. Posada, *Environ. Sci.: Water Res. Technol.*, 2020, **6**, 877–910.
16 M. Silva, J. P. Baltrus, D. J. Burnett and J. Baltrusaitis, *ACS Earth Space Chem.*, 2022, **6**, 431–443.
17 Y. Luo, H. Li, Y.-R. Huang, T.-L. Zhao, Q.-Z. Yao, S.-Q. Fu and G.-T. Zhou, *Chem. Eng. J.*, 2018, **351**, 195–202.
18 D. Kiani, Y. Sheng, B. Lu, D. Barauskas, K. Honer, Z. Jiang and J. Baltrusaitis, *ACS Sustainable Chem. Eng.*, 2018, **7**, 1545–1556.
19 N. Park, H. Chang, Y. Jang, H. Lim, J. Jung and W. Kim, *Water Sci. Technol.*, 2020, **81**, 2511–2521.

20 M. Silva, V. Murzin, L. Zhang, J. P. Baltrus and J. Baltrusaitis, *Environ. Sci.: Nano*, 2020, **7**, 3482–3496.
21 B. Lu, D. Kiani, W. Taifan, D. Barauskas, K. Honer, L. Zhang and J. Baltrusaitis, *J. Phys. Chem. C*, 2019, **123**(14), 8908–8922.
22 D. Kiani, M. Silva, Y. Sheng and J. Baltrusaitis, *J. Phys. Chem. C*, 2019, **123**, 25135–25145.
23 J. Pesonen, P. Myllymäki, S. Tuomikoski, G. Vervecken, T. Hu, H. Prokkola, P. Tynjälä, U. Lassi, J. Pesonen, P. Myllymäki, S. Tuomikoski, G. Vervecken, T. Hu, H. Prokkola, P. Tynjälä and U. Lassi, *ChemEngineering*, 2019, **3**, 40.
24 L. Chen, C. H. Zhou, H. Zhang, D. S. Tong, W. H. Yu, H. M. Yang and M. Q. Chu, *Chemosphere*, 2017, **187**, 302–310.
25 U. J. Kim, J. K. Oh and K. Kannan, *Environ. Sci. Technol.*, 2017, **51**, 7872–7880.
26 Q. Zhang, S. Zhao, X. Ye and W. Xiao, *Desalin. Water Treat.*, 2016, **57**, 10924–10933.
27 A. Rabinovich and A. A. Rouff, *ACS ES&T Water*, 2021, **1**, 910–918.
28 Z. L. Ye, Y. Deng, Y. Lou, X. Ye, J. Zhang and S. Chen, *Chem. Eng. J.*, 2017, **313**, 1633–1638.
29 Q. L. Chen, X. L. An, Y. G. Zhu, J. Q. Su, M. R. Gillings, Z. L. Ye and L. Cui, *Environ. Sci. Technol.*, 2017, **51**, 8149–8157.
30 M. A. De Boer, C. Kabbe and J. C. Slootweg, *Environ. Sci. Technol.*, 2018, **52**, 14564–14565.
31 T. G. Bekele, H. Zhao, Q. Wang and J. Chen, *Environ. Sci. Technol.*, 2019, **53**, 13417–13426.
32 A. Blum, M. Behl, L. S. Birnbaum, M. L. Diamond, A. Phillips, V. Singla, N. S. Sipes, H. M. Stapleton and M. Venier, *Environ. Sci. Technol. Lett.*, 2019, **6**, 638–649.
33 A. K. Greaves and R. J. Letcher, *Environ. Sci. Technol.*, 2014, **48**, 7942–7950.
34 Q. Zhang, Y. Yao, Y. Wang, Q. Zhang, Z. Cheng, Y. Li, X. Yang, L. Wang and H. Sun, *Environ. Pollut.*, 2021, **288**, 117742.
35 L. Y. Kuo and N. M. Perera, *Inorg. Chem.*, 2000, **39**, 2103–2106.
36 L. Poirier, L. Plener, D. Daudé and E. Chabrière, *Sci. Rep.*, 2020, **10**, 1–11.
37 C. Pope, *Encycl. Toxicol. Third Ed.*, 2014, pp. 759–761.
38 G. A. Petroianu, M. Y. Hasan, K. Arafat, S. M. Nurulain and A. Schmitt, *J. Appl. Toxicol.*, 2005, **25**, 562–567.
39 W. Y. Xie, Q. Shen and F. J. Zhao, *Eur. J. Soil Sci.*, 2018, **69**, 181–195.
40 J. Rivera-Utrilla, M. Sánchez-Polo, M. Á. Ferro-García, G. Prados-Joya and R. Ocampo-Pérez, *Chemosphere*, 2013, **93**, 1268–1287.
41 K. E. O'Shea and D. D. Dionysiou, *J. Phys. Chem. Lett.*, 2012, **3**, 2112–2113.
42 Y. Zhu, R. Zhu, Y. Xi, J. Zhu, G. Zhu and H. He, *Appl. Catal., B*, 2019, **255**, 117739.
43 M. Silva and J. Baltrusaitis, *J. Hazard. Mater. Lett.*, 2021, **2**, 100012.
44 E. Yamal-Turbay, E. Jaén, M. Graells and M. Pérez-Moya, *J. Photochem. Photobiol., A*, 2013, **267**, 11–16.
45 M. Silva, J. P. Baltrus, C. Williams, A. Knopf, L. Zhang and J. Baltrusaitis, *Appl. Catal., A*, 2022, **630**, 118468.
46 S. Xin, G. Liu, X. Ma, J. Gong, B. Ma, Q. Yan, Q. Chen, D. Ma, G. Zhang, M. Gao and Y. Xin, *Appl. Catal., B*, 2021, **280**, 119386.
47 J. Feng, X. Hu and L. Y. Po, *Environ. Sci. Technol.*, 2004, **38**, 5773–5778.
48 P. Stolzenburg, A. Capdevielle, S. Teychené and B. Biscans, *Chem. Eng. Sci.*, 2015, **133**, 9–15.
49 S. K. L. Ishii and T. H. Boyer, *Water Res.*, 2015, **79**, 88–103.
50 T. Zhang, L. Ding and H. Ren, *J. Hazard. Mater.*, 2009, **166**, 911–915.
51 M. M. Rahman, M. A. M. Salleh, U. Rashid, A. Ahsan, M. M. Hossain and C. S. Ra, *Arabian J. Chem.*, 2014, **7**, 139–155.
52 Y. S. Ho and G. McKay, *Process Biochem.*, 1999, **34**, 451–465.
53 J. P. Gustafsson, *Visual MINTEQ 3.0 user guide*, 2011, pp. 1–73.
54 M. Silva, J. Baltrus, C. Williams, A. Knopf, L. Zhang and J. Baltrusaitis, *J. Environ. Chem. Eng.*, 2021, **9**, 105589.
55 M. Fang, R. Zheng, Y. Wu, D. Yue, X. Qian, Y. Zhao and Z. Bian, *Environ. Sci.: Nano*, 2019, **6**, 105–114.
56 G. A. El-Shobaky, M. Mokhtar and A. M. Salem, *Mater. Res. Bull.*, 2005, **40**, 891–902.
57 H. S. Liu, K. J. Wang, X. Y. Cao, J. X. Su and Z. Gu, *RSC Adv.*, 2021, **11**, 12532–12542.
58 D. A. Svintsitskiy, T. Y. Kardash, O. A. Stonkus, E. M. Slavinskaya, A. I. Stadnichenko, S. V. Koscheev, A. P. Chupakhin and A. I. Boronin, *J. Phys. Chem. C*, 2013, **117**, 14588–14599.
59 D. Zhao, C.-M. Tu, X.-J. Hu and N. Zhang, *RSC Adv.*, 2017, **7**, 37596–37603.
60 S. H. Lee, B. H. Yoo, S. J. Lim, T. H. Kim, S. K. Kim and J. Y. Kim, *J. Cryst. Growth*, 2013, **372**, 129–137.
61 C. Fang, T. Zhang, R. Jiang and H. Ohtake, *Sci. Rep.*, 2016, **6**, 1–10.
62 R. Khamizov, D. A. Sveshnikova, A. E. Kucherova and L. A. Sinyaeva, *Russ. J. Phys. Chem. A*, 2018, **92**, 1451–1460.
63 Y. Wang, L. Rao, P. Wang, Z. Shi and L. Zhang, *Appl. Catal., B*, 2020, **262**, 118308.
64 N. Barhoumi, N. Oturan, S. Ammar, A. Gadri, M. A. Oturan and E. Brillas, *Environ. Chem. Lett.*, 2017, **15**, 689–693.
65 M. Pirsaheb, S. Moradi, M. Shahlaei and N. Farhadian, *New J. Chem.*, 2020, **44**, 17735–17743.
66 Y. Y. Chen, Y. L. Ma, J. Yang, L. Q. Wang, J. M. Lv and C. J. Ren, *Chem. Eng. J.*, 2017, **307**, 15–23.
67 V. S. Birchal, S. D. F. Rocha, M. B. Mansur and V. S. T. Ciminelli, *Can. J. Chem. Eng.*, 2001, **79**, 507–511.
68 J. A. Mejias, A. J. Berry, K. Refson and D. G. Fraser, *Chem. Phys. Lett.*, 1999, **314**, 558–563.
69 G. L. Smithson and N. N. Bakhshi, *Can. J. Chem. Eng.*, 1969, **47**, 508–513.
70 P. Xia, X. Wang, X. Wang, J. Song, H. Wang and J. Zhang, *Colloids Surf., A*, 2016, **506**, 220–227.
71 J. Li, X. Wang, J. Wang, Y. Li, S. Xia and J. Zhao, *Chem. Eng. J.*, 2019, **362**, 802–811.
72 R. C. de S. Meira, S. P. A. da Paz and J. A. M. Corrêa, *J. Mater. Res. Technol.*, 2020, **9**, 15202–15213.

73 M. Dindarsafa, A. Khataee, B. Kaymak, B. Vahid, A. Karimi and A. Rahmani, *Ultrason. Sonochem.*, 2017, **34**, 389–399.
74 A. E. Johnston and I. R. Richards, *Soil Use Manage.*, 2003, **19**, 45–49.
75 M. Markovic, B. O. Fowler and M. S. Tung, *J. Res. Natl. Inst. Stand. Technol.*, 2004, **109**, 553.
76 R. L. Frost, M. L. Weier, W. N. Martens, D. A. Henry and S. J. Mills, *Spectrochim. Acta, Part A*, 2005, **62**, 181–188.
77 V. Stefov, B. Šoptrajanov, I. Kuzmanovski, H. D. Lutz and B. Engelen, *J. Mol. Struct.*, 2005, **752**, 60–67.
78 D. Sidorczuk, M. Kozanecki, B. Civalleri, K. Pernal and J. Prywer, *J. Phys. Chem. A*, 2020, **124**, 8668–8678.
79 E. Yakubovskaya, T. Zaliznyak, J. Martínez Martínez and G. T. Taylor, *Sci. Rep.*, 2019, **9**, 15785.
80 T. Zhang, C. Fang, P. Li and R. F. Jiang, *Adv. Mater. Res.*, 2014, **955**, 1983–1986.
81 C. Leypold, M. Reiher, G. Brehm, M. Schmitt, S. Schneider, P. Matousek and M. Towrie, *Phys. Chem. Chem. Phys.*, 2003, **5**, 1149–1157.
82 M. Muhammad, B. Yan, G. Yao, K. Chao, C. Zhu and Q. Huang, *ACS Appl. Nano Mater.*, 2020, **3**, 7066–7075.
83 J. Zhao, P. Liu, H. Yuan, Y. Peng, Q. Hong and M. Liu, *J. Spectrosc.*, 2016, **2016**, 1845237.